

Non-isothermal phase-field simulations of laser-written in-plane SiGe heterostructures for photonic applications

Ozan Aktas¹, Yuji Yamamoto², Mehmet Kaynak² & Anna C. Peacock¹

Advanced solid-state devices, including lasers and modulators, require semiconductor heterostructures for nanoscale engineering of the electronic bandgap and refractive index. However, existing epitaxial growth methods are limited to fabrication of vertical heterostructures grown layer by layer. Here, we report the use of finite-element-method-based phase-field modelling with thermocapillary convection to investigate laser inscription of in-plane heterostructures within silicon-germanium films. The modelling is supported by experimental work using epitaxially-grown $\text{Si}_{0.5}\text{Ge}_{0.5}$ layers. The phase-field simulations reveal that various in-plane heterostructures with single or periodic interfaces can be fabricated by controlling phase segregation through modulation of the scan speed, power, and beam position. Optical simulations are used to demonstrate the potential for two devices: graded-index waveguides with Ge-rich (>70%) cores, and waveguide Bragg gratings with nanoscale periods (100–500 nm). Periodic heterostructure formation via sub-millisecond modulation of the laser parameters opens a route for post-growth fabrication of in-plane quantum wells and superlattices in semiconductor alloy films.

¹Optoelectronics Research Centre, University of Southampton, Southampton, UK. ²IHP-Leibniz-Institut für Innovative Mikroelektronik, Frankfurt (Oder), Germany. ✉email: O.Aktas@soton.ac.uk; acp@orc.soton.ac.uk

Modern-day applications of microelectronics, optoelectronics, and photonics have become undoubtedly possible with the technological advancements in material growth and formation of interfaces between different materials. For example, the development of semiconductor heterostructures, quantum wells, and superlattices, which provide confinement for light and carriers via spatially engineered refractive index and bandgap profiles, has enabled the fabrication of various devices such as heterojunction bipolar transistors, double heterojunction lasers, quantum cascade lasers, distributed Bragg reflectors, semiconductor saturable absorber mirrors, and modulators^{1–5}. Methods commonly used to grow epitaxial layers of semiconductors are molecular beam epitaxy and derivatives of chemical vapor deposition (CVD), which allow for material growth with atomic precision and control^{6,7}. However, these methods implement a layer-by-layer growth approach; therefore, they can only be used to fabricate vertical heterostructures and superlattices, which are limited in total thickness ($< 5 \mu\text{m}$) due to the constraint of lattice matching and strain issues⁸. Recently, fabrication of lateral and axial heterostructures have been demonstrated in semiconductor alloys of nanoribbons^{9,10}, and nanowires^{11,12}, respectively, by switching the precursors during material growth on planar substrates. However, a versatile strategy to fabricate in-plane heterostructures, quantum wells, and superlattices within semiconductor alloy films has yet to be demonstrated.

As an alternative heterostructure formation, post-process approaches such as thermally-induced phase segregation have been applied to induce axial and lateral heterostructures in initially homogeneous alloys of nanowires¹³, and monolayers¹⁴, respectively. Similar manifestations of phase segregation resulting in quasi-regular in-plane heterostructures have also been observed in semiconductor superlattices due to the strain-induced lateral compositional self-modulation¹⁵, and directionally solidified alloys where banding occurs due to oscillations in the speed of the solidification front near the instability regime¹⁶. However, because of their spontaneous and elusive nature, it is challenging to control these effects to form heterostructures within semiconductor alloy films. Generally, phase segregation is an undesired phenomenon for epitaxial growth of heterostructures in semiconductor alloy epilayers. This is particularly true for silicon-germanium (SiGe) alloys¹⁷, which have a large gap between the liquidus and solidus curves in the phase diagram¹⁸.

For stable growth from a melted SiGe alloy where phase segregation results in a Ge-rich liquid phase, solidification speeds have to be smaller than a critical speed, which depends on the local temperature gradient and thermophysical properties of the alloy. Otherwise, constitutional undercooling can emerge ahead of the solid/liquid interface, breaking its stability¹⁹. Consequently, the interface instability results in cellular or faceted structures during bulk crystal growth^{20–22}, and dendritic structures during laser annealing of SiGe films on glass substrates^{23–25}, leading to a random redistribution of the initial composition. To exploit heat-induced phase segregation for the fabrication of regular in-plane heterostructures with well-defined morphologies, cellular, or dendritic solidification of alloy thin films needs to be avoided by ensuring either low growth speeds or high temperature gradients at the liquid/solid interface. However, low solidification speeds, on the order of $10 \mu\text{m s}^{-1}$ to allow for stable growth, are impractical in terms of process time. Another alternative is the application of non-conventional thermal sources, like lasers, to post-process semiconductor alloy thin films grown on substrates with high thermal conductivities^{26,27}. Such methods allow for achieving extremely high temperature gradients (10^9K m^{-1}), which are required to ensure the stability of the solid/liquid interface. Recently, by using laser processing of amorphous SiGe

thin films on silicon substrates, the fabrication of polycrystalline SiGe microstripes was demonstrated with compositional profiles that can be tuned by applying different scan speeds in the range of $0.1\text{--}100 \text{mm s}^{-1}$ ²⁸. Additionally, it is known from classical theory of solidification that transient effects such as acceleration of the liquid/solid interface can be used to form compositional microstructures²⁹, and this was recently demonstrated by laser processing of SiGe core silica cladding fibers³⁰.

Over the past two decades, phase-field models have been extensively applied to study the formation of cellular and dendritic structures during solidification of alloys^{31–34}, where a phase-field parameter $\phi(\mathbf{r}, t)$ is used to track the liquid/solid interface. Here, we extend these studies to show that it can also be exploited for modeling non-dendritic solidification of laser-melted semiconductor alloys. A three-dimensional (3D) finite-element-method (FEM)-based phase-field model was used to investigate non-isothermal solidification with thermocapillary convection, and motional effects on phase segregation at the moving liquid/solid interface. The simulation results are supported with experimental data, which were obtained by optical microscopy and scanning transmission electron microscopy (STEM) with energy-dispersive X-ray spectroscopy (EDX), using $\text{Si}_{0.5}\text{Ge}_{0.5}$ alloy thin films epitaxially grown on silicon substrates. Based on this, we introduce a concept for post-process laser writing of in-plane heterostructures with single or periodic interfaces in semiconductor alloy epilayers. Our work focuses on SiGe epilayers because of the increasing interest in Ge/SiGe heterostructures in micro/nanostructures³⁵, and their tantalizing prospect for quantum cascade lasers³ and parabolic quantum wells³⁶, etc. However, our method can be applied to pseudo-binary alloys of other materials, such as ternary semiconductors ($\text{Al}_x\text{Ga}_{1-x}\text{As}$) with phase diagrams similar to that of SiGe (see Supplementary Fig. 1). The potential to use laser-written in-plane SiGe heterostructures for photonic applications is demonstrated via FEM-based optical simulations of two proposed devices: i) graded-index waveguides for mid-infrared (mid-IR) photonic applications, and ii) waveguide Bragg gratings for wavelength filtering in the mid-IR spectrum.

Results

Laser writing of in-plane longitudinal SiGe heterostructures with tunable compositionally-graded profiles at various constant scan speeds. We begin our investigations of laser-driven heterostructure formation with some preliminary experimental work by applying laser processing on homogeneous 575 nm thick SiGe epilayers (50% Ge). The $\text{Si}_{0.5}\text{Ge}_{0.5}$ epilayers were epitaxially grown on silicon substrates by reduced pressure CVD³⁷. For laser processing, we used a continuous wave laser operating at 532 nm and an experimental setup schematically shown in Supplementary Fig. 2. The laser beam with a power of 2.5 W was focused to a spot with a diameter of $5 \mu\text{m}$ on the surface of the $\text{Si}_{0.5}\text{Ge}_{0.5}$ epilayer by a $10\times$ microscope objective. Laser processing was conducted at the same power with different constant scan speeds in the range of $0.1\text{--}200 \text{mm s}^{-1}$. Scanning the stage under the fixed laser beam produces a traveling molten zone. Depending on the scan speed, the laser-driven liquid/solid interface produces microstripes solidified with varying Ge compositions, as shown in the optical microscope image in Fig. 1a. The laser-written SiGe microstripes for the low scan speeds of 0.1 and 1mm s^{-1} are barely distinguishable; however, wider microstripes emerge with a yellow color as the scan speed increases and Ge accumulates on the surface.

Phase-field simulations of laser-written in-plane longitudinal SiGe heterostructures. We carried out 3D FEM-based non-

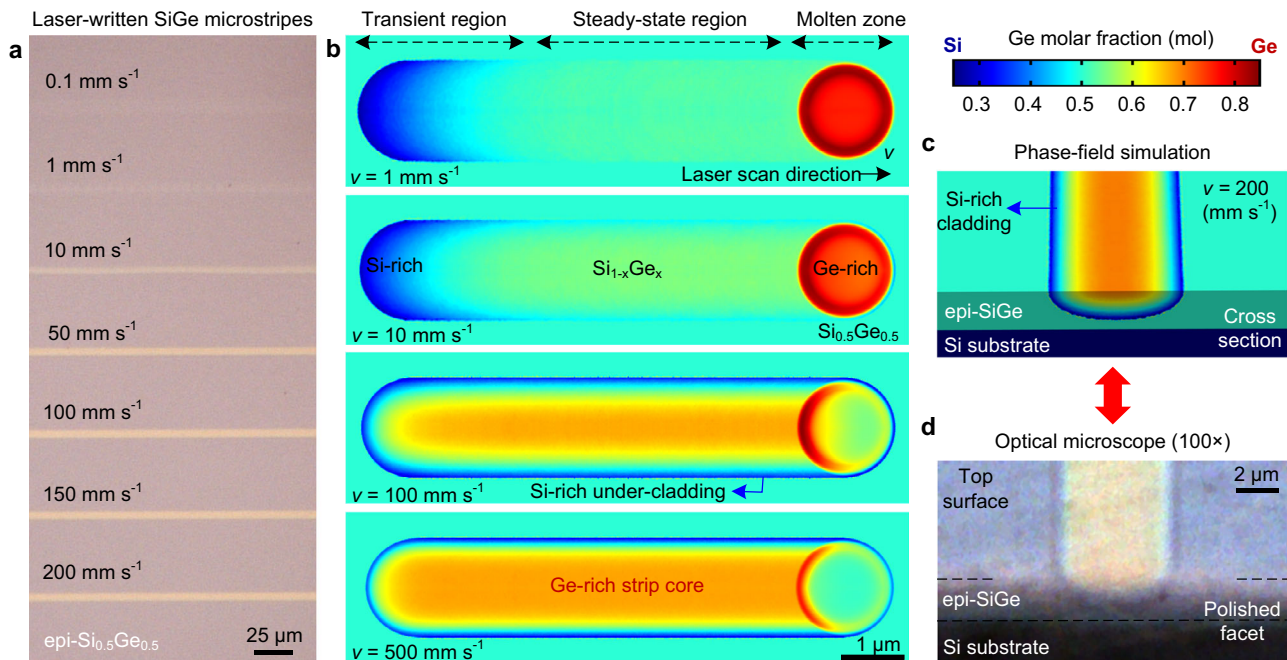


Fig. 1 Laser writing of in-plane longitudinal SiGe heterostructures via scan-speed-dependent spatial redistribution of the composition. **a** Optical microscope image showing laser-written microstripes on a $\text{Si}_{0.5}\text{Ge}_{0.5}$ thin film (epi-SiGe) epitaxially grown on Si substrates, for scan speeds in the range of $0.1\text{--}200\text{ mm s}^{-1}$. **b** Results of finite-element-method (FEM)-based phase-field simulations for laser-driven phase segregation are given as composition color maps showing the Ge molar fraction $x(\mathbf{r})$ for the short transient (blue) and indefinitely-long steady-state regions (yellow/orange) solidified behind the laser-induced molten zone (red) traveling at a constant scan speed in the range of $1\text{--}500\text{ mm s}^{-1}$. **c** Simulated spatial redistribution of the alloy composition in the cross-section and on the top surface of a laser-written microstripe. An in-plane longitudinal SiGe heterostructure was formed with a Ge-rich strip core and Si-rich under-cladding along the scan direction. The image size in the transverse direction was rescaled accordingly to match the width of the laser-written microstripes in **d**. **d** Optical microscope image showing the angle-polished cross-section and top facet of a longitudinal SiGe heterostructure laser-written at 200 mm s^{-1} for qualitative comparison with the simulation result.

isothermal phase-field simulations to compare with the experimental results. To understand the effect of the thermocapillary convection on the distribution of composition within the molten zone, the Navier–Stokes equations (Eqs. (12, 13) in the “Methods” section) were solved concurrently with the segregation-diffusion-convection equation and heat transport equation (Eqs. (20, 31), respectively, in the “Methods” section). To reduce the simulation volume, we chose a beam spot size of $2\text{ }\mu\text{m}$ and a scan range of $10\text{ }\mu\text{m}$, which are smaller compared to the experimental parameters. The other parameters used in the simulations were: optical power of 200 mW , scan speeds in the range of $1\text{--}500\text{ mm s}^{-1}$, and a $\text{Si}_{0.5}\text{Ge}_{0.5}$ epilayer (epi-SiGe) with a thickness of 500 nm . We also assumed that the thermal properties of the $\text{Si}_{0.5}\text{Ge}_{0.5}$ alloy, such as the melting temperature and thermal conductivity are determined by the initial composition $x_0 = 0.5$, and stay constant during the simulations. The values used for the material and thermal properties of the SiGe alloys were taken from the literature (see Supplementary Table 1). Further details regarding the implementation of the phase-field simulations in COMSOL are given in Supplementary Note 1.

The simulation results (see Fig. 1b) show the spatial redistribution of the Ge molar fraction x within the laser-processed microstripes at various scan speeds. The laser-induced molten zone (red) travels along the scan direction dragging the Ge-rich liquid, and solidifies at the trailing edge with a scan-speed-dependent redistribution of the initial composition $x_0 = 0.5$. After a short Si-rich transient (blue), an indefinitely long steady-state region emerges with a Ge-rich ($x > 0.5$) strip core (yellow) and a Si-rich ($x < 0.5$) under-cladding. The phase-field modeling provides good qualitative agreement when compared to the experimental observations of the scan-speed-dependent Ge redistribution. For

example, both the experimental data given in Fig. 1a and the simulation results given in Fig. 1b show that the Ge-rich strip core on the top surface widens as the scan speed increases. For further qualitative comparison, a laser-processed SiGe epilayer was cleaved in the middle, and its cleaved edge was polished at an angle to reveal the cross-section of a longitudinal heterostructure laser-written at a scan speed of 200 mm s^{-1} . The simulated redistribution of the composition on the top surface and in the cross-section (see Fig. 1c) agrees well with the experimental result shown in the optical microscope image in Fig. 1d. The Ge-rich top surface (yellow) and boundary of the Si-rich cladding (blue) are clearly observable via the natural color contrast.

The simulation results show that the laser beam absorbed by the SiGe epilayer increases the surface temperature up to $1475\text{ }^\circ\text{C}$, resulting in a molten zone and a thermocapillary-driven convection. The size of the molten zone, and thermocapillary-driven flow pattern were found to be quite similar for the experimental scan speed range, as the maximum experimental scan speed v of 200 mm s^{-1} is one order of magnitude smaller than the maximum flow speed $u_{\text{max}} = 2.3\text{ m s}^{-1}$. In Fig. 2a, the phase field parameter $\phi(\mathbf{r})$ shows the solid regions (blue) and molten zone (red) traveling at a scan speed of 1 mm s^{-1} . The solid/liquid interface (rainbow color) has a depth-dependent thickness ranging between $60\text{--}125\text{ nm}$, due to the different thermal gradients, and mushy zone between the liquidus and solidus curves in the phase diagram. The thermocapillary convection within the molten zone pushes the liquid radially outwards from the center (see Fig. 2b), forming a Ge-rich stagnant layer (darker red) close to the liquid/solid interface, where the flow speed decreases to 0 m s^{-1} from the maximum value of 2.3 m s^{-1} . Therefore, distribution of the composition in

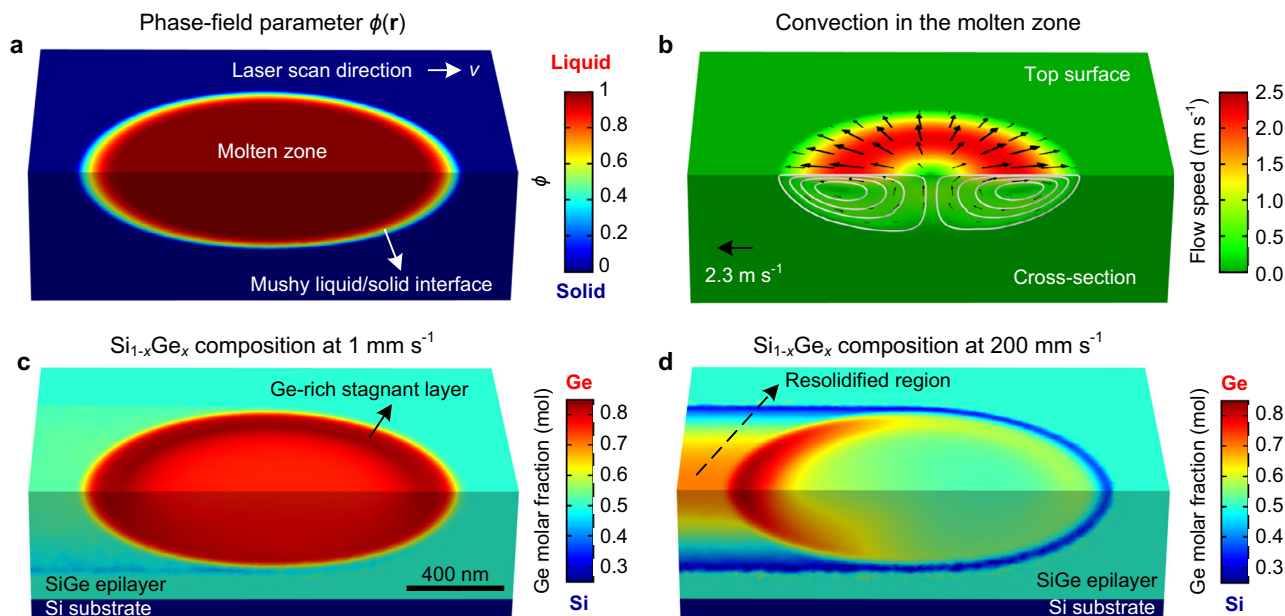


Fig. 2 Phase-field parameter $\phi(\mathbf{r})$, thermocapillary convection and distribution of the alloy composition in the laser-induced molten zone traveling in the scan direction. **a** Phase-field parameter $\phi(\mathbf{r})$ shows the liquid (red) and solid (blue) phases with a mushy interface (rainbow color) in a laser-processed SiGe epilayer. **b** Thermocapillary-driven convection within the traveling molten zone, which is shown here only for a scan speed of 1 mm s^{-1} . The white lines and black arrows represent streamlines of the fluid flow and instantaneous flow velocity, respectively. The scan-speed-dependent Ge distribution within the molten zone is shown in composition color maps for **c** low and **d** high scan speeds.

the Ge-rich molten zone is not homogeneous (see Fig. 2c). At high scan speeds, a build-up of Ge occurs at the trailing edge (see Fig. 2d), because of insufficient diffusion-limited transport preventing complete mixing in the annular stagnant layer, as in the case for low scan speeds. By leveraging the scan-speed-dependent phase segregation, different Ge profiles in the laser-processed region can thus be obtained.

The Ge concentration profiles calculated by the phase-field simulations along different directions at the top surface and cross-section are given in Fig. 3a–c for the in-plane longitudinal SiGe heterostructures laser-written at different scan speeds. When the laser beam melts the surface and induces phase segregation at the liquid/solid interface, the excess Ge abruptly diffuses into the molten zone, due to the higher solubility of Ge in the liquid phase. As the laser beam moves in the scan direction, more Ge accumulates in the molten zone up to a steady-state composition. Therefore, the Ge concentration of the initially solidified material in the transient region is very low (see Fig. 3a). However, it increases remarkably as the steady-state composition is reached in the Ge-rich molten zone. The length of the transient region highly depends on the scan speed. The higher Ge content in the stagnant layer close to the liquid/solid interface can also be seen in Fig. 3a. A maximum Ge molar fraction x up to 0.7 mol is reached on the top surface in the steady-state region for the scan speed of 200 mm s^{-1} . Higher scan speeds result in the levelling off of the Ge composition, widening the width of the Ge-rich strip core, as shown in Fig. 3b for the scan speed of 500 mm s^{-1} . The phase-field gradient $\nabla\phi$ has the highest value at the bottom of the molten zone, which increases the strength of phase segregation according to Eq. (20). Thus, more Ge diffuses away from the liquid/solid interface, and the most Si-rich region in the undercladding occurs at the bottom close to the SiGe/Si interface (see Fig. 3c). The effect of laser driven phase segregation on the dispersion of the Ge molar fraction can be clearly seen by calculating histograms of the composition within the entire solidified volume in the steady-state region for different scan speeds (Fig. 3d). These results complement our understanding of

the formation of in-plane longitudinal heterostructures using laser processing.

Our FEM-based approach was not limited by the RAM memory ($<100 \text{ GB}$), but by the total time (>2 days) required to run each phase-field simulation with thermocapillary convection. It is for this reason that we were only able to simulate laser processing using laser-written stripes with smaller sizes ($2 \mu\text{m}$ wide and $10 \mu\text{m}$ long) compared to the experimentally measured sizes ($5.7 \mu\text{m}$ wide and 4 cm long). Therefore, this does not allow for a one-to-one quantitative comparison between the experiments and the simulation results given in Fig. 3a–c. However, to reduce the total simulation time significantly so that these can be conducted with the experimental cross-sectional dimensions, the thermocapillary-driven convection can be neglected in the phase-field simulations by not incorporating the Navier–Stokes equations. This is justified as the absence of the convection (see Supplementary Fig. 3) would only result in a slightly higher Ge content ($\Delta x < 0.02 \text{ mol}$) at the center of the top surface. This difference is experimentally insignificant as the achievable compositional resolution is typically on the order of 0.05 mol (5%)²⁸.

To conduct the comparison, the cross-section of a SiGe microstripe laser-written at a scan speed of 200 mm s^{-1} , was analysed using STEM with EDX. A high-angle annular dark-field (HAADF) image, which was taken with $\times 14,000$ magnification of the cross-section at 200 keV , shows the material contrast in Fig. 4a, due to the redistribution of the composition in the melted region, as given by the two-dimensional (2D) EDX map in Fig. 4b. Our simulated result, neglecting thermocapillary convection but using the actual experimental thickness of the SiGe epilayer (575 nm) and width of the laser-written stripe ($5.7 \mu\text{m}$), is shown in Fig. 4c, revealing the 2D redistribution of Ge in the cross-section. The 1D concentration depth profile was also calculated and compared with the EDX data in Fig. 4d, which was compensated for the presence of other impurity elements, such as oxygen and carbon. The simulated 2D and 1D Ge profiles agree quantitatively well with the EDX data, which has an error margin

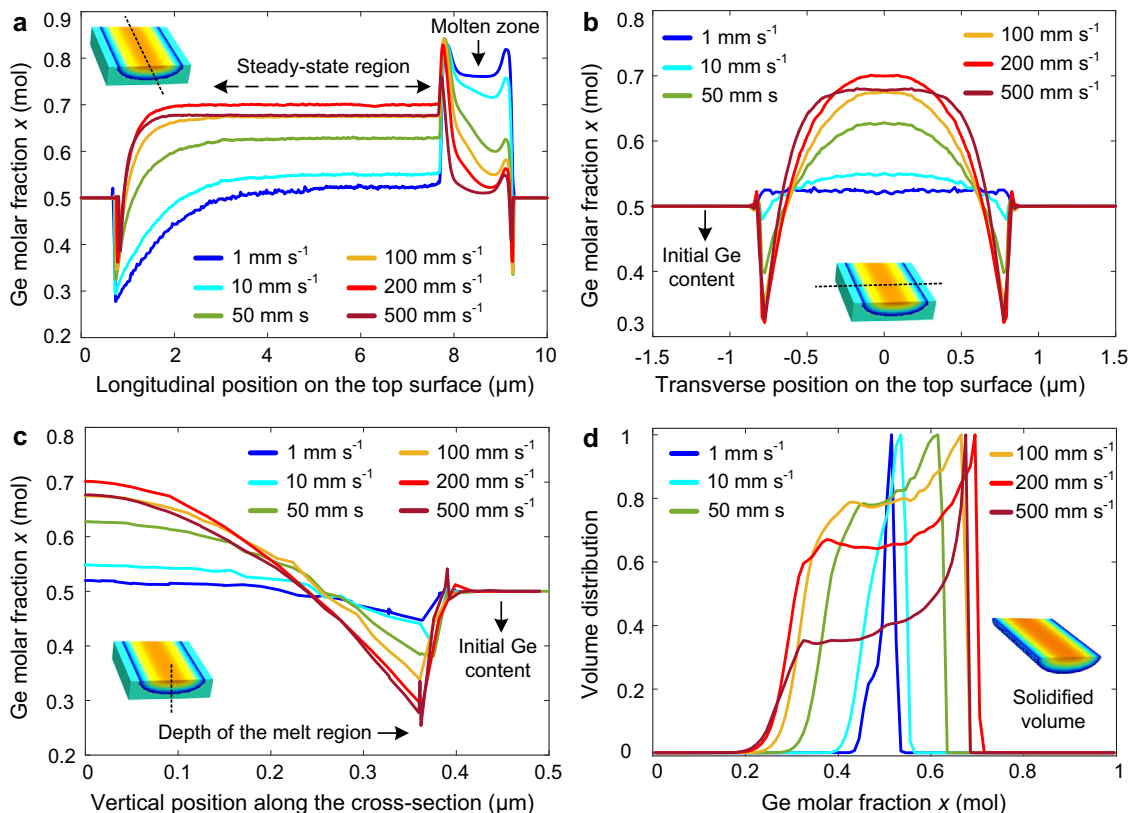


Fig. 3 Simulation results showing the $\text{Si}_{1-x}\text{Ge}_x$ composition profiles along different directions on various surfaces, and dispersion of the composition for scan speeds in the range of $1\text{--}500\text{ mm s}^{-1}$. Inset figures show the surface and direction (dotted lines) where the composition profile was taken. Ge molar fraction $x(r)$ along the **a** longitudinal and **b** transverse directions on the top surface, and **c** along the vertical direction at the cross-sections of laser-written SiGe microstrips. **d** Normalized volume histogram showing the scan-speed-dependent dispersion of the initial composition $x_0 = 0.5$ within the whole solidified volume in terms of the Ge molar fraction. The bin size for histograms is $\Delta x = 0.01$. Inset figure shows the laser-processed volume in the steady-state region, where the histograms were calculated.

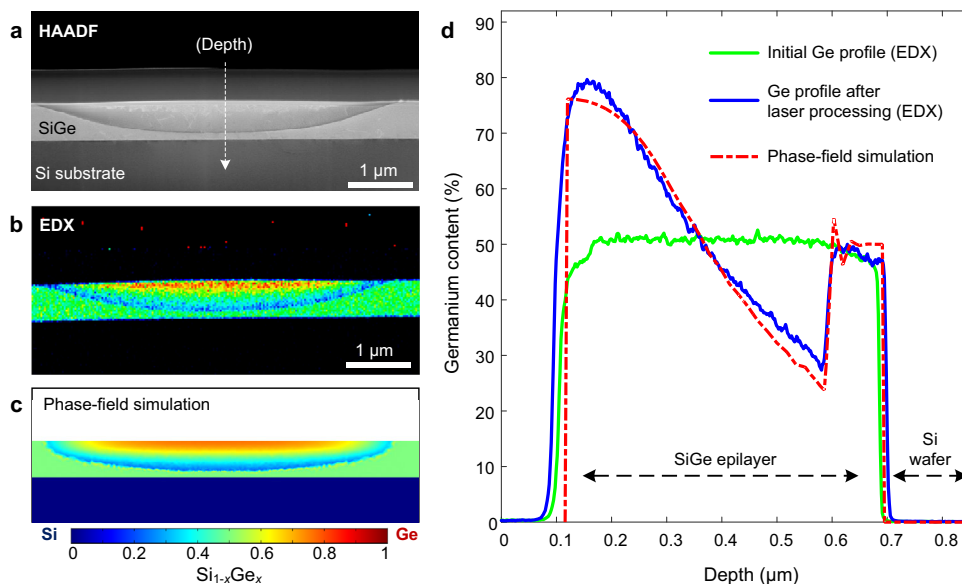


Fig. 4 Elemental analysis of an in-plane longitudinal SiGe heterostructure laser-written at a scan speed of 200 mm s^{-1} . **a** High-angle annular dark-field image (HAADF) showing the material contrast at the cross-section of the laser-processed region. **b** Energy-dispersive X-ray spectroscopy (EDX) and **c** phase-field simulation results showing spatial redistribution of the alloy composition at the cross-section for 2D comparison. The color scale applies to both figures in **b**, **c**. **d** Quantitative comparison between the experimental (blue solid line) and simulated (red dashed line) Ge concentration along the depth profile across the cross-section, as marked by a white arrow in **a**. The experimental error margin in the EDX data is 5%.

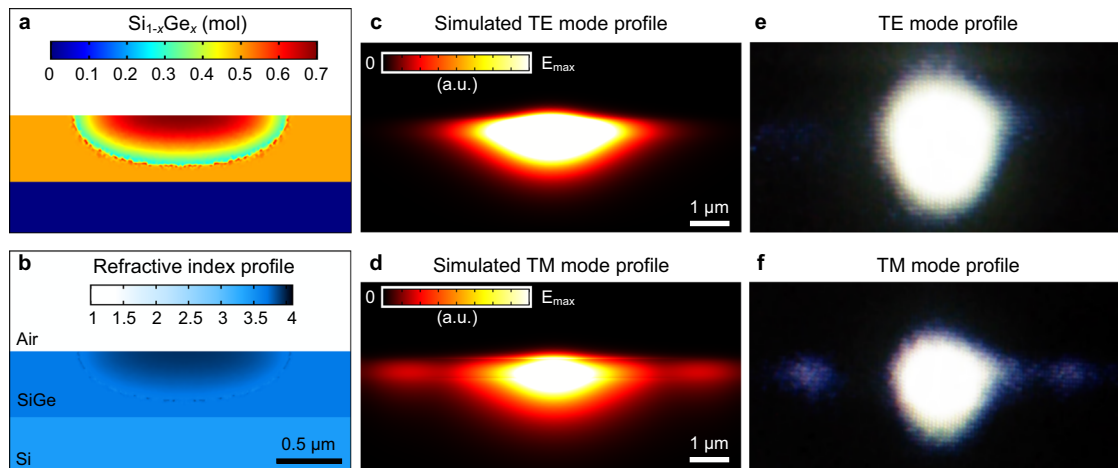


Fig. 5 Laser-written in-plane longitudinal SiGe heterostructures as graded-index optical waveguides. **a** Simulated spatial redistribution of Ge molar fraction $x(\mathbf{r})$ and **b** calculated refractive index $n(x)$ of the cross-section of a SiGe heterostructure laser-written at a scan speed of 200 mm s^{-1} . Simulated **c** transverse electric (TE) and **d** transverse magnetic (TM) polarized mode profiles obtained by modal analysis using the refractive index profile $n(\mathbf{r})$ in **b**. Infrared (IR) camera image showing the experimentally captured intensity profiles for the **e** TE and **f** TM polarized modes of light, which was free space coupled into the 1 cm long laser-written SiGe waveguides using a fiber laser emitting at $2 \mu\text{m}$.

of $\pm 5\%$. It is worth noting that even in the case of laser processing at a scan speed of 200 mm s^{-1} , where the maximum compositional segregation occurs, the Ge concentration profile is smoothly changing across the cross-section, as can be seen in Fig. 4d. However, an abrupt transition occurs within a 25 nm range at the melt/solid boundary, jumping from the lowest Ge content (25%) to the initial Ge content (50%) of the SiGe epilayer.

Modal analysis of in-plane longitudinal SiGe heterostructures that function as laser-written graded-index waveguides. Similar to the double heterostructure semiconductor lasers, where optical guiding is achieved in a high-index core sandwiched between two lower index claddings, a single longitudinal heterostructure formed with a Ge-rich stripe core and a surrounding Si-rich cladding can provide confinement for light. To illustrate this concept, we calculated the optical modes supported by a longitudinal heterostructure laser-written at a scan speed of 200 mm s^{-1} by a focused beam of $2 \mu\text{m}$ in diameter. The 2D Ge molar fraction at the cross-section of the laser-written SiGe microstripe, which was obtained by a phase-field simulation, is given in Fig. 5a. The corresponding refractive index profile $n(x)$ at a wavelength of $2 \mu\text{m}$ was calculated by using $n(x) = 3.451 + 0.2951x + 0.3419x^2$, which is a quadratic function of the Ge molar fraction³⁸.

The process temperatures, which are high enough to melt the surface, result in biaxial tensile strains within the laser-processed SiGe films, due to the difference between the thermal expansion coefficients of Ge and Si. Residual tensile strains as high as 0.6% can be reached²⁸. Therefore, photo-elastic effects, which are strain-induced changes in the refractive index n , need to be incorporated³⁹. We found that an increase of 3% in the refractive index within the laser-processed strained region gives the best agreement with the optical experiments in terms of matching the mode profiles. The resulting refractive index profile, which includes the photo-elastic effects, is shown in Fig. 5b. The simulated fundamental mode profiles for the transverse electric (TE) and transverse magnetic (TM) polarized light at a wavelength of $2 \mu\text{m}$ are shown in Fig. 5c, d, respectively.

For a proof-of-principle demonstration, we used a 1 cm long SiGe microstripe that was written using a laser with a spot size of $5 \mu\text{m}$ at a scan speed of 200 mm s^{-1} . The end facets were prepared for optical coupling by manual cleaving, and a $2 \mu\text{m}$ fiber laser was first free space coupled into the graded-index SiGe

waveguide by using a $60\times$ objective. The light at the output was then collimated by a $40\times$ objective and imaged by an infrared camera to capture the images of the TE and TM modes shown in Fig. 5e, f, respectively. A schematic for the experimental setup used for optical coupling is given in Supplementary Fig. 4. In agreement with the optical simulations, we observed that only the fundamental TE and TM modes were guided through these laser-written SiGe waveguides at a wavelength of $2 \mu\text{m}$. Moreover, optical guiding was observed even for the waveguide written at the lowest scan speed of 0.1 mm s^{-1} , where the least compositional segregation occurs within the laser-processed region. This observation confirms our assumption that the residual tensile strains increase the refractive index in the laser-processed regions to allow for optical guiding. The TM mode was found to be lossy; therefore, it leaks from the strip core decreasing the intensity of the propagating light. More confinement is necessary for the TM mode to achieve optical guiding at much longer wavelengths, such as in the molecular fingerprint regime ($6\text{--}20 \mu\text{m}$ wavelength). The depth of the melted region is naturally limited by the thickness of the SiGe epilayer, which can be grown on a Si substrate with a thickness up to $10 \mu\text{m}$ using CVD methods. By increasing the laser power and using longer wavelengths ($>532 \text{ nm}$), the deposited energy and optical penetration can be increased to deepen the melted region closer to the SiGe/Si interface.

Conventional waveguides depend on patterning of silicon-on-insulator (SOI) wafers by e-beam lithography and etching. Although this approach provides compact components for integrated photonics in the telecom range, the silica buffer oxide layer in SOI waveguides suffers from strong absorption above $3.6 \mu\text{m}$, hindering photonic applications in the mid-IR range. Therefore, graded-index SiGe waveguides have recently received increased interest for mid-IR applications in integrated photonics^{40,41}, due both to the low optical losses ($1\text{--}2 \text{ dB cm}^{-1}$) in the wavelength range of $2\text{--}8 \mu\text{m}$ and their tunable optical properties via compositional engineering. However, these graded-index SiGe waveguides fabricated by epitaxial growth have two drawbacks: i) The graded refractive index can only be obtained in the growth direction perpendicular to the substrate surface, and a step index profile in the plane for mode confinement still requires patterning of the surface similar to the SOI waveguides. ii) Waveguides with different graded index profiles on the same

substrate require different growth processes for each of them, increasing the cost and complexity of the fabrication. In contrast, for the laser-written graded-index SiGe waveguides, an index grading both in the transverse and vertical directions at the cross-section is simultaneously achieved via compositional segregation of the alloy within the melt region during laser processing. Moreover, this graded index profile is tunable by controlling the laser scan speed, allowing fabrication of customized waveguides using the same homogeneous SiGe epilayer grown on a Si substrate. A tunable index profile can be leveraged for dispersion engineering in nonlinear optical applications. Furthermore, compositional segregation of Si and Ge enables a refractive index difference Δn on the order of 10^{-1} , which is higher compared to those typically obtained (10^{-4}) in laser-written waveguides in bulk unary semiconductors via pulsed-laser-induced modifications⁴². Furthermore, laser writing of SiGe waveguides does not require lithographic patterning, which can lead to scattering losses due to the roughness of the etched waveguide boundaries, and it can be used to write components with complex shapes such as directional couplers, Y-junctions, S-bends, and spirals, if 2-axis motorized stages are used⁴³.

Phase-field simulations of in-plane periodic transverse heterostructures (superlattices) fabricated by modulation of the laser processing parameters. As the steady-state region within the laser-written microstripes is indefinitely long (depending only on the total scan range), the laser processing parameters can be modulated to create transient effects superimposed on the constant scan speed of the stage during laser processing. To investigate the idea, we first performed simulations with the modulation of the stage scan speed to produce periodic heterostructures in the steady-state region (see Fig. 1b). A 77.6 kHz square wave modulation of the stage scan speed v between 25–50 mm s^{-1} with a duty cycle of 1/3 resulted in a SiGe superlattice with a period of $\Lambda = 430$ nm (see Fig. 6a). The resulting periodic composition profile is embedded into the Ge-rich strip core and diminishes close to the surrounding Si-rich cladding (down to a depth of 300 nm), as shown in the inset figure. The composition profile (blue) along the longitudinal direction on the top surface shows the profile of the Ge molar fraction, where the stationary background composition level is determined by the initial scan speed (see Fig. 3a). It is possible to obtain a higher background composition level up to the maximum Ge molar fraction of $x = 0.7$ by increasing the initial scan speed; however, this requires application of higher modulation frequencies to achieve the same period. To demonstrate a smaller period and a different background composition level, we performed a 621.1 kHz modulation of the stage scan speed v between 100–200 mm s^{-1} , which forms a SiGe superlattice with a period of $\Lambda = 220$ nm, as shown in Fig. 6b. Although smaller periods down to 100 nm could be achieved, the finiteness of the mesh (minimum 20 nm) limits the resolution of the simulated heterostructures.

Modulation of the scan speed by controlling the movement of the stage, where the SiGe sample is fixed, might be experimentally limited by the maximum achievable acceleration due to the inertia of the stage mechanism. Much faster motional transients for the laser-induced molten zone can be realized by modulating either power or position of the laser beam using electro-optic modulators/deflectors or acousto-optic scanners, while the stage moves independently at a constant scan speed. We performed 20% modulation (reduction) of the laser power $P_0 = 200$ mW with a duty cycle of 1/3 at 61.0 kHz to obtain an in-plane transverse SiGe superlattice with a period of $\Lambda = 402$ nm (see Fig. 6c). In this case, we were able to obtain a greater change in the Ge molar fraction in the range of $\Delta x = 0.55$ – 0.78 mol, via the

higher acceleration of the solidification boundary when the spot size suddenly shrinks. Another approach for modulation is switching the position of the focused laser beam back and forth in the scan direction while the stage moves at a constant scan speed. A 61.1 kHz sawtooth modulation of the beam position with a movement of 200 nm resulted in a SiGe superlattice with a period of $\Lambda = 410$ nm (see Fig. 6d). Slowing the speed of the laser beam in the return cycle helps to lower the Ge molar fraction (down to $x_0 = 0.5$) between the two maxima of the composition. Periodic heterostructure formation via modulation of the beam position and power are shown in Supplementary Movies 1 and 2, respectively.

Optical simulations for transmission and reflection spectra of waveguide Bragg gratings based on in-plane transverse SiGe superlattices. Waveguide Bragg gratings, which consist of alternating layers with different refractive indices, is one of the basic elements used in integrated photonics today. Primary methods used to fabricate Bragg gratings are material removal by etching⁴⁴, and local refractive index modification induced by ultra-fast lasers⁴⁵. Laser-written in-plane transverse SiGe superlattices can be exploited as a waveguide Bragg grating if the period Λ of the grating satisfies the first-order Bragg condition $\lambda = 2n_{\text{eff}}\Lambda$, where λ is the wavelength of interest, and n_{eff} is the effective index of the reflected optical mode.

We simulated an in-plane transverse SiGe superlattice laser-written at a constant stage scan speed of 25 mm s^{-1} , using a sawtooth modulation of the laser beam position with a movement of 200 nm (see Fig. 7a). A 10-period Bragg grating with a period of $\Lambda_0 = 285$ nm was chosen for a filtering application at a wavelength range around 2 μm . The total length of the Bragg grating was kept short, due to the computational constraints of the FEM-based optical simulations in 3D. However, to increase the coupling between propagating and counter-propagating modes in such a short waveguide Bragg grating, we ensured that the maximum refractive index modulation was achieved in the periodic composition profile ($\Delta x = 0.45$ – 0.75 mol), as shown in Fig. 7b. The calculated transmission and reflection spectra of the 10-period waveguide Bragg grating are shown in Fig. 7c. Further details regarding implementation of the optical simulations are given in Supplementary Note 2.

A dip in the transmission spectrum was observed at a wavelength of 2038.9 nm for the reflected TE mode with an effective index of $n_{\text{eff}} = 3.5244$. By using the Bragg condition, we found that this corresponds to a period Λ of 289.3 nm, which is close to the simulated period $\Lambda_0 = 285$ nm. A slight mismatch is expected due to the coarser size of the mesh (40 nm) used for the optical simulations. Additionally, we noticed that the reflection was suppressed, which is desired for a notch filter application. The reduction in the reflection is common for single mode waveguides with asymmetric gratings, like a tilted fiber Bragg grating, which couple the reflected light into higher order lossy modes. As our graded-index SiGe waveguides support only the fundamental TE mode at a wavelength of 2000 nm, we expect high losses for the reflected higher order modes. A waveguide Bragg grating with a high number of periods (>1000) and a longer total length (>300 μm) would be straightforward to fabricate to achieve better rejection ratios in the stop band, and thus could find ready use in integrated photonics applications.

Discussion

Laser-driven phase segregation in homogeneous $\text{Si}_{0.5}\text{Ge}_{0.5}$ epilayers allows for achieving Ge concentrations remarkably higher ($x > 0.7$) and lower ($x < 0.25$) than the initial concentration within the strip core and under-cladding, respectively. To obtain higher

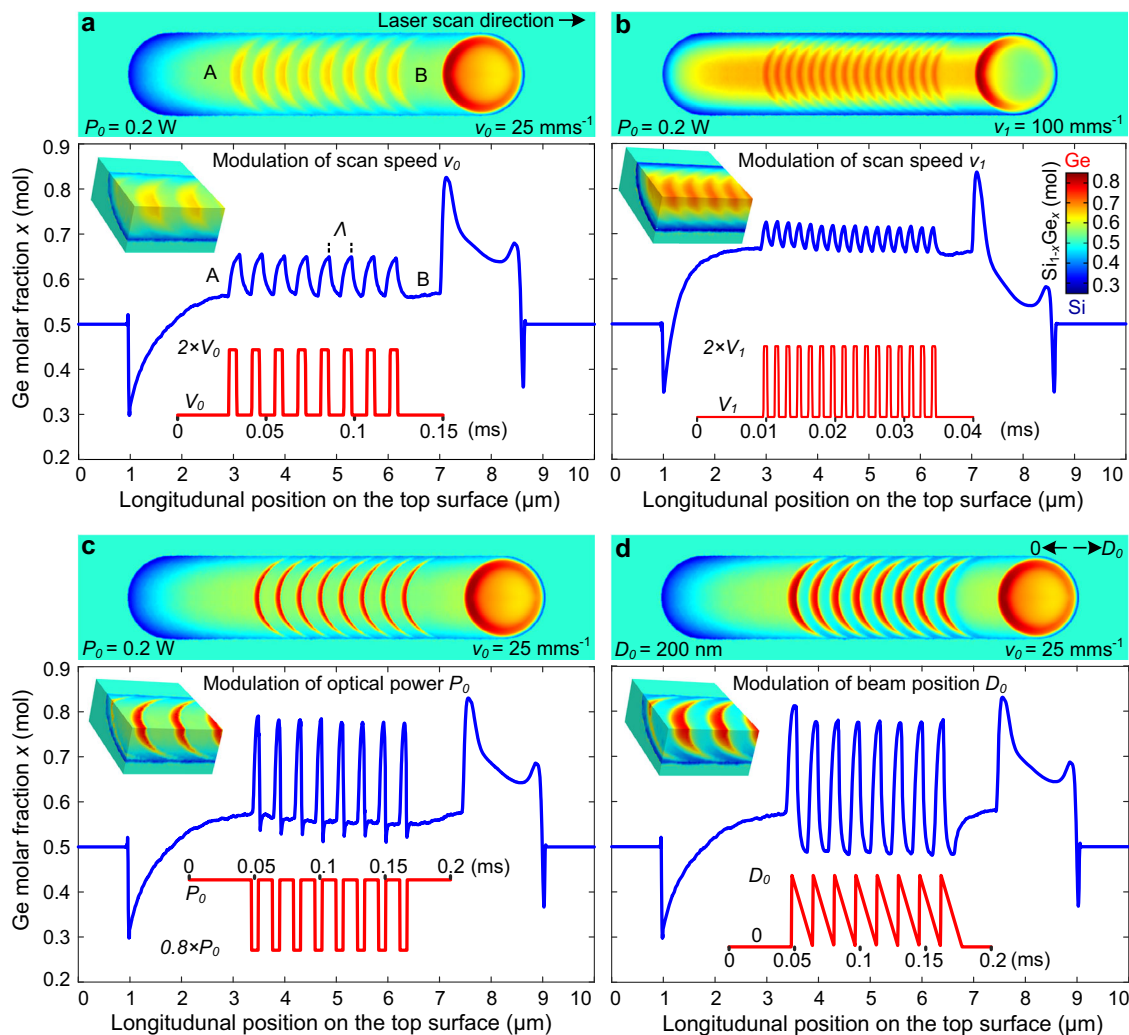


Fig. 6 Laser-written in-plane transverse SiGe superlattices fabricated by sub-millisecond modulation of the scan speed, optical power, and beam position. Composition color maps show the Ge molar fraction x on the top surface of the laser-written microstrips. Inset figures show the periodic composition distributions at the transverse and longitudinal cross-sections to reveal the depth of the modulated regions. Modulated laser processing parameters and resulting composition profiles on the top surface are given in red and blue colors, respectively. All square wave modulations have a duty cycle of $1/3$. **a** A 77.6 kHz square wave modulation of the stage scan speed v between 25–50 mm s^{-1} results in an in-plane SiGe superlattice with a period of $\Lambda = 430$ nm. **b** 621.1 kHz modulation of the stage scan speed v between 100–200 mm s^{-1} forms a SiGe superlattice with a period of $\Lambda = 220$ nm. **c** While the stage moves at a constant speed of 25 mm s^{-1} , 61.0 kHz 20% modulation (reduction) of the laser power $P_0 = 0.2$ W forms a SiGe superlattice with a period of $\Lambda = 402$ nm. **d** 61.1 kHz sawtooth wave modulation of the beam position with a back-and-forth movement of 200 nm forms a SiGe superlattice with a period of $\Lambda = 410$ nm. The color scale applies to all composition maps.

Ge concentrations, SiGe epilayers with an initially higher Ge content can be used. According to our phase-field simulations, laser processing of a SiGe epilayer with an initial 80% Ge content at a scan speed of 200 mm s^{-1} enables a 95% Ge content to be reached at the top surface of the strip core. The initial Ge content can be further increased, however, the strength of the phase segregation decreases due to narrowing of the gap between the liquid and solidus curves in the phase diagram. In contrast, using transient effects such as the acceleration of the liquid/solid boundary via modulation of the laser processing parameters has a stronger effect in terms of reaching a higher Ge content. This could potentially lead to the fabrication of in-plane transverse heterostructures having pure Ge in Ge-rich SiGe epilayers, which are in high demand for development of spin-based quantum technologies⁴⁶, as well as for fabrication of quantum wells and superlattices, which could be used as building blocks of photonic and optoelectronic devices including photodetectors and modulators.

To further control the transverse patterning, laser beam shapes can be used to obtain non-circular beam shapes. For example, in-plane transverse heterostructures with straight interfaces perpendicular to the scan direction, required for quantum well-like structures, could be written using a rectangular-shaped laser beam. Although the transverse size of the periodic heterostructures is determined by the diameter of the focused laser spot, the spatial period is not diffraction-limited. This is because it is not the spot area⁴⁷, but the displacement of the 2D liquid/solid interface in the scan direction that determines the period, which in principle can be as small as the modulation frequency of the laser processing parameters can be increased. Thus, the width of the quantum wells that could be written into the epilayers is determined by multiplication of the constant scan speed and modulation period Δt . For example, to fabricate a quantum well with a width of 20 nm, the modulation period should be 1 μs for a scan speed of 20 mm s^{-1} . This corresponds to a modulation frequency of 1 MHz, which is within the capabilities of state-of-

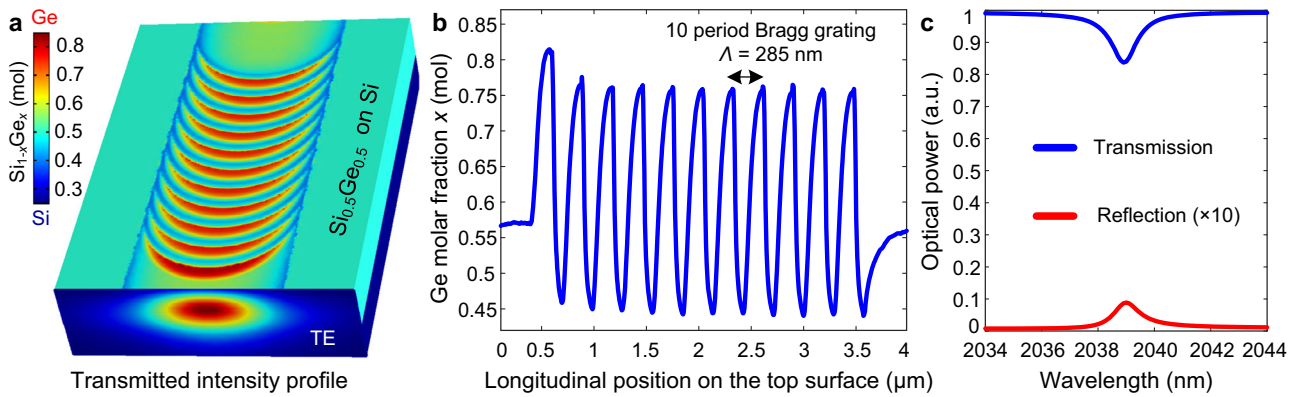


Fig. 7 Laser-written in-plane transverse SiGe superlattice on a silicon substrate as a waveguide Bragg grating. **a** Composition color map shows the periodic Ge molar fraction x on the top surface of an in-plane transverse SiGe superlattice written at a constant stage scan speed of 25 mm s^{-1} , using a sawtooth wave modulation of the laser beam position (back and forth movement of 200 nm) in the scan direction. Calculated optical intensity profile of a transverse electric (TE) polarized mode is shown as superimposed on the output facet of the simulated waveguide Bragg grating. **b** Ge molar fraction profile as a function of position along the center line on the top surface showing a 10-period grating with a period of 285 nm . **c** Calculated transmission and reflection spectra of the 10-period SiGe waveguide Bragg grating by using finite-element-method (FEM)-based optical simulations. The reflection data (red bottom line) is magnified ten times for clarity.

the-art electro-optic laser beam modulators and deflectors. However, the estimated average thickness of the mushy solid/liquid interface is 90 nm , which depends on the local thermal gradients, and mushy zone range at $x_0 = 0.5$. Therefore, we expect that the width of the quantum wells could be decreased further by setting the spatial period of the modulation smaller than 90 nm . However, this would compromise the modulation depth Δx in composition, which is the maximum compositional difference between the well and barrier regions. It is worth noting that these laser-written in-plane transverse heterostructures do not have an atomically-sharp interface, but a gradual one, which could be useful to fabricate graded confining potentials³⁶.

For the fabrication of active devices based on in-plane heterostructures, a doping process is required. Conventionally, doping can be realized after laser processing by either ion-implantation or thermally assisted diffusion from a dopant source. However, this would compromise the crystalline structure and Ge profile of the superlattices, decreasing the compositional contrast between the well and barrier regions. SiGe epilayers can also be doped during epitaxial growth via CVD. Laser post-processing can be then applied to these initially doped SiGe epilayers to fabricate in-plane doped heterostructures. The most appealing aspect of this strategy would be simultaneous activation of the dopants without requiring an additional annealing process, though it could also result in a redistribution of the dopants within the heterostructures. Another useful avenue to explore would be to populate un-doped Ge-rich heterostructures with charge carriers by either using modulation doping or gate-induced accumulation from the ohmic contacts⁴⁶. Finally, laser-driven phase segregation with modulation of the laser process parameters could also be applied to fabricate in-plane heterostructures in other pseudo-binary systems, such as metal alloys (Ni-Cu), ternary semiconductor alloys ($\text{Al}_x\text{Ga}_{1-x}\text{As}$), quaternary alloys of transition metal dichalcogenides ($\text{Mo}_x\text{W}_{1-x}\text{S}_y\text{Se}_{1-y}$)¹⁴, and ceramics ($\text{Al}_2\text{O}_3\text{-Cr}_2\text{O}_3$), which have phase diagrams similar to that of SiGe alloy.

Methods

Calculation of the equilibrium phase diagram for SiGe alloys. We used the molar Gibbs free energy F to calculate the equilibrium phase diagram of SiGe alloys. By fitting it to the experimental phase diagram data, we estimated the parameters in the molar Gibbs free energy $F(\phi, T, x)$, which is given at a constant

volume and a constant pressure for a regular solution model of binary alloys by⁴⁸,

$$\begin{aligned} F(\phi, T, x) &= E(\phi, T, x) - TS(E(\phi, T, x), \phi, x), \\ &= (1-x)F_{\text{Si}}(\phi, T) + xF_{\text{Ge}}(\phi, T) \\ &\quad + RT[(1-x)\ln(1-x) + x\ln(x)] + w(\phi)x(1-x), \end{aligned} \quad (1)$$

where $E(\phi, T, x)$ is the total internal energy, $S(E(\phi, T, x), \phi, x)$ is the total entropy, T is the temperature, x is the molar fraction of Ge, R is the ideal gas constant, ϕ is the phase-field representing the solid ($\phi = 0$) and liquid ($\phi = 1$) phases. $F_{\text{Si}}(\phi, T)$ and $F_{\text{Ge}}(\phi, T)$ are the Gibbs free energies in units of J mol^{-1} for pure Si and Ge, respectively. The molar Gibbs free energy for a pure element A (Si or Ge) is given by⁴⁹,

$$F_A(\phi, T) = E_A(\phi, T) - TS_A(\phi, T) = H_{\text{Ag}}(\phi) + L_A \left(1 - \frac{T}{T_m^A}\right) p(\phi) + F_{\text{A,Solid}}, \quad (2)$$

where $E_A(\phi, T)$ and $S_A(\phi, T)$ are the internal energy and entropy for the pure element A, respectively; H_A is the height of the energy barrier between the liquid and solid phases at the melting temperature T_m^A ; L_A is the latent heat of melting; $g(\phi) = \phi^2(1-\phi)^2$ is the double-well potential function with minima at $\phi = 0$ and $\phi = 1$; and $p(\phi) = \phi^2(3-2\phi)$ is an interpolating function, which satisfies $p(\phi = 0) = 0$ and $p(\phi = 1) = 1$. The height of the energy barrier H_A is assumed to be the same for Si and Ge, due to the similar atomic properties. $F_{\text{A,Solid}}$ is the Gibbs free energy of the solid pure element A, which is assumed to be zero. The last term in Eq. (1) is the molar excess Gibbs free energy, which is proportional to the parameter $w(\phi)$ given by

$$w(\phi) = w_S(1-\phi) + w_L\phi, \quad (3)$$

where w_S and w_L are regular solution parameters corresponding to solid and liquid phases of the SiGe alloy, respectively.

The chemical potentials μ for Si and Ge can be calculated from the molar Gibbs energy $F(\phi, T, x)$ in Eq. (1) as:⁵⁰

$$\mu_{\text{Si}}(\phi, T, x) = F - x \frac{\partial F}{\partial x} = w(\phi)x^2 + F_{\text{Si}}(\phi, T) + RT \ln(1-x), \quad (4)$$

$$\mu_{\text{Ge}}(\phi, T, x) = F + (1-x) \frac{\partial F}{\partial x} = w(\phi)(1-x)^2 + F_{\text{Ge}}(\phi, T) + RT \ln(x). \quad (5)$$

In the case of phase coexistence at thermal equilibrium, the chemical potential for each element in the solid (S) and liquid (L) solutions are equal, and given by

$$\mu_{\text{Si}}^S(\phi = 0, T, x_S) = \mu_{\text{Si}}^L(\phi = 1, T, x_L), \quad (6)$$

$$\mu_{\text{Ge}}^S(\phi = 0, T, x_S) = \mu_{\text{Ge}}^L(\phi = 1, T, x_L), \quad (7)$$

where x_S and x_L are the Ge molar fractions in the solid and liquid solutions of $\text{Si}_{1-x}\text{Ge}_x$, respectively. By using Eqs. (2-7) can be rewritten explicitly in terms of the regular solution parameters, latent heats of melting, and melting temperatures of the alloy elements⁵⁰, as given below

$$\ln \frac{1-x_S}{1-x_L} = \frac{L_{\text{Si}}}{R} \left(\frac{1}{T} - \frac{1}{T_m^{\text{Si}}} \right) + \frac{1}{RT} (w_L x_L^2 - w_S x_S^2), \quad (8)$$

$$\ln \frac{x_S}{x_L} = \frac{L_{Ge}}{R} \left(\frac{1}{T} - \frac{1}{T_m^{Ge}} \right) + \frac{1}{RT} [w_L(1-x_L)^2 - w_S(1-x_S)^2], \quad (9)$$

which are implicit analytic expressions for the liquidus $x_L(T)$ and solidus $x_S(T)$ curves in the phase diagram of SiGe. As shown in Supplementary Fig. 1, the best fitting parameters (normalized by the ideal gas constant R) for the experimental phase diagram were found to be $T_m^{Si} = 1687$ K, $L_{Si}/R = 6040$ K, $T_m^{Ge} = 1211$ K, $L_{Ge}/R = 4441$ K, $w_S/R = 450$ K and $w_L/R = 800$ K.

Thermocapillary-driven convection in the laser-induced molten zone.

Buoyancy-driven convection within the laser-induced melt pool was neglected because the highest temperature is reached on the top surface, where the fluid with the lowest density already resides. In contrast, the thermocapillary effect (Marangoni effect), which is due to the temperature-dependent surface tension $\sigma(T)$, is the dominant driving force for the convection, which can result in fluid flows with maximum speeds u_{max} in a range of 1–10 m s⁻¹ for semiconductors melted by lasers^{51,52}. The laser-processed SiGe films were treated as a highly viscous liquid with a dynamic viscosity $\mu(\phi)$ varying by several orders of magnitude between the solid phase ($\mu_S = 1.0 \times 10^3$ N s m⁻²) and liquid phase ($\mu_L = 0.8 \times 10^{-3}$ N s m⁻²), which is given in the form

$$\mu(\phi) = \mu_L p(\phi) + \mu_S (1 - p(\phi)), \quad (10)$$

where $p(\phi)$ is the interpolation function. The surface tension σ for the liquid SiGe alloy, which was estimated using the surface tensions of liquid Si and Ge⁵³, is assumed to be a linear function of temperature T as

$$\sigma(T) = 0.653(N m^{-1}) - 10^{-4}(N m^{-1} K^{-1})[T - T_m], \quad (11)$$

where T_m is the melting temperature of the alloy.

To describe fluid motion in the molten pool due to the thermocapillary convection, we solved Navier–Stokes equations, which in a general form read as

$$\nabla \cdot (\rho \mathbf{u}) = 0, \quad (12)$$

$$\rho \frac{\partial \mathbf{u}}{\partial t} + \rho(\mathbf{u} \cdot \nabla) \mathbf{u} = \nabla \cdot [-\rho \mathbf{I} + \mu(\nabla \mathbf{u} + \nabla \mathbf{u}^T)] + F, \quad (13)$$

where ρ is the fluid density, \mathbf{u} is the velocity field, p is the dynamic pressure, \mathbf{I} is the unity tensor, and F is a source term representing body sources, such as gravity force. We also assumed a laminar incompressible flow ($\nabla \cdot \mathbf{u} = 0$) for the simulations. The thermocapillary effect is a shear stress, which depends on the tangential temperature gradient, and it was implemented as a surface boundary condition

$$[-\rho \mathbf{I} + \mu(\nabla \mathbf{u} + \nabla \mathbf{u}^T)] \cdot \mathbf{n} = \gamma[\nabla T - \mathbf{n}(\mathbf{n} \cdot \nabla T)], \quad (14)$$

where \mathbf{n} is the vector normal to the fluid surface, and $\gamma = d\sigma/dT$ is the temperature derivative of the surface tension σ in Eq. (11).

Non-isothermal phase-field formulation of the segregation-diffusion-convection equation and heat transport equation.

To describe the laser melting process, a segregation-diffusion-convection equation needs to be formulated incorporating phase segregation in the laser-melted SiGe epilayers, as well as the convection in the molten pool, which is driven mainly by the thermocapillary effect. For a thermodynamically consistent derivation of a non-isothermal phase-field model⁵⁴, we postulate an entropy functional \hat{S} defined by the integral of the entropy density $s(e, \phi, x)$ over the whole SiGe epilayer volume, as given by

$$\hat{S} = \int \left[s(e, \phi, x) - \frac{\epsilon_c^2}{2} |\nabla e|^2 - \frac{\epsilon_x^2}{2} |\nabla x|^2 - \frac{\epsilon_\phi^2}{2} |\nabla \phi|^2 \right] dV, \quad (15)$$

where e is the energy density, $\phi(\mathbf{r}, t)$ is the phase-field parameter representing the solid domains and traveling molten zone in the Si_{1-x}Ge_x epilayer. The gradient coefficient ϵ_x is generally required at very high scan speeds (>1 m s⁻¹), where the characteristic length L_s of the solute boundary layer approaches atomic dimensions and solidification occurs without redistribution of the composition (partitionless solidification). However, L_s is 60 nm for our maximum scan speed of 0.5 m s⁻¹, thus ϵ_x could be neglected. ϵ_e was also neglected as it is not part of the conventional heat transport equation, which will be derived in the following paragraphs. ϵ_ϕ , which is related to the thickness and energy of the solid/liquid interface, was assumed to be constant.

Time-dependent equations, which ensure positive local entropy production according to the laws of thermodynamics⁴⁸, can be derived for the Ge molar fraction, energy density, and phase-field parameter as

$$\frac{\partial x}{\partial t} = -\nabla \cdot \left[M_x \nabla \left(\frac{\partial s}{\partial x} \right) \right] = \nabla \cdot \left[M_x \nabla \left(\frac{1}{T} \frac{\partial f}{\partial x} \right) \right], \quad (16)$$

$$\frac{\partial e}{\partial t} = -\nabla \cdot \left[M_e \nabla \left(\frac{\partial s}{\partial e} \right) \right] = -\nabla \cdot \left[M_e \nabla \left(\frac{1}{T} \right) \right], \quad (17)$$

$$\frac{\partial \phi}{\partial t} = M_\phi \left[\frac{\partial s}{\partial \phi} + \epsilon_\phi^2 \nabla^2 \phi \right] = -M_\phi \left[\frac{1}{T} \frac{\partial f}{\partial \phi} - \epsilon_\phi^2 \nabla^2 \phi \right], \quad (18)$$

where M_e , M_x , and M_ϕ are positive-definite parameters, and $T(\mathbf{r}, t)$ is the temperature field. In the kinetic equations in Eqs. (16–18), the partial derivatives of the entropy density s are rewritten in terms of the partial derivatives of the free energy density $f(\phi, T, x)$, which is in units of J m⁻³ and derived from the molar Gibbs free energy F given in Eq. (1), divided by the molar volume V_m of the SiGe alloy:

$$f(\phi, T, x) = \frac{F(\phi, T, x)}{V_m}, \quad (19)$$

By adding a conservative convection term $\nabla \cdot (\mathbf{u} x)$ on the left-hand side of Eq. (16), a segregation-diffusion-convection equation is finally derived as,

$$\frac{\partial x}{\partial t} + \nabla \cdot (\mathbf{u} x) = \nabla \cdot \left\{ M_x \left[\frac{\partial}{\partial x} \left(\frac{1}{T} \frac{\partial f}{\partial x} \right) \nabla x + \frac{\partial}{\partial \phi} \left(\frac{1}{T} \frac{\partial f}{\partial x} \right) \nabla \phi + \frac{\partial}{\partial T} \left(\frac{1}{T} \frac{\partial f}{\partial x} \right) \nabla T \right] \right\}. \quad (20)$$

Here, $\partial f / \partial x$ is calculated from Eqs. (1, 19) as

$$\frac{\partial f}{\partial x} = \frac{1}{V_m} \left\{ \left[L_{Ge} \left(1 - \frac{T}{T_m^{Ge}} \right) - L_{Si} \left(1 - \frac{T}{T_m^{Si}} \right) \right] p(\phi) + RT \ln \left(\frac{x}{1-x} \right) + w(\phi)(1-2x) \right\}. \quad (21)$$

To ensure a composition independent diffusion coefficient D , the mobility M_x is taken as

$$M_x = \frac{D(\phi)T}{\partial^2 f(\phi, T, x) / \partial x^2} = \frac{V_m D(\phi) T (1-x)x}{RT - 2x(1-x)w(\phi)}, \quad (22)$$

where the phase-dependent diffusion coefficient is

$$D(\phi) = D_S(1-\phi) + D_L\phi. \quad (23)$$

The diffusion coefficients in the liquid and solid SiGe phases are taken as $D_L = 3.0 \times 10^{-8}$ m² s⁻¹ and $D_S = 10^{-16}$ m² s⁻¹, respectively. When $\nabla \phi = 0$ and $\nabla T = 0$, the standard diffusion equation is obtained, as the Ge concentration C is related to the Ge molar fraction x by $C = x/V_m$.

By using Eqs. (1, 2, and 19), the energy density of a partially-melted alloy can be written as⁴⁸,

$$e(x, \phi, T) = (1-x)e_{Si}(\phi, T) + xe_{Ge}(\phi, T) + w(\phi)x(1-x), \quad (24)$$

where e_{Si} and e_{Ge} are energy densities of pure Si and Ge. For a pure element A (Si or Ge), we assume that e_A can be written as,

$$e_A(\phi, T) = e_{A,S}(T)(1-\phi) + e_{A,L}(T)\phi, \quad (25)$$

where $e_{A,S}$ and $e_{A,L}$ are the energy densities of the solid and liquid phases of the pure element. By inserting Eqs. (3, 25) into Eq. (24), the energy density of the alloy can be rewritten as

$$e(x, \phi, T) = \left[(1-x)e_{Si,S}(T) + xe_{Ge,S}(T) + w_S(1-x)x \right] (1-\phi) + \left[(1-x)e_{Si,L}(T) + xe_{Ge,L}(T) + w_L(1-x)x \right] \phi. \quad (26)$$

The terms in the square brackets in Eq. (26) are defined as h_S and h_L for the solid and liquid phases of the alloy, respectively, to obtain a compact form for the energy density, which is rewritten as:

$$e(x, \phi, T) = h_S(x, T)(1-\phi) + h_L(x, T)\phi. \quad (27)$$

These terms depend on the composition and temperature, as implied by Eq. (26). The composition is determined by the initial Ge fraction x_0 of the initially-homogeneous alloy. To simplify the implementation of the simulations, we assume the x -dependent terms in h_S and h_L stay constant in the following derivation. Furthermore, the density ρ of the SiGe alloy is also assumed to be constant (temperature independent) and the same for both phases.

For derivation of a heat transport equation⁵⁵, by inserting Eq. (27) into Eq. (17), we obtain

$$\rho \left[\frac{1}{\rho} \frac{dh_S}{dT} (1-\phi) + \frac{1}{\rho} \frac{dh_L}{dT} \phi \right] \frac{dT}{dt} + \rho \left[\frac{(h_L - h_S)}{\rho} \frac{d\phi}{dT} \right] \frac{dT}{dt} = \nabla \cdot \frac{M_e}{T^2} \nabla T, \quad (28)$$

where the density of the alloy is inserted to convert the energy density to energy per mass. Equation (28) can then be recast into the conventional heat transport equation as

$$\rho \left[c_{p,S}(1-\phi) + c_{p,L}\phi + L \frac{d\phi}{dT} \right] \frac{dT}{dt} = \nabla \cdot k \nabla T. \quad (29)$$

Here, $k = M_e/T^2$ is the thermal conductivity, and $c_{p,S}$ and $c_{p,L}$ are the specific heat capacity of the solid and liquid phases, respectively. The terms in the square parenthesis can be defined as an apparent heat capacity c_p

$$c_p = c_{p,S}(1-\phi) + c_{p,L}\phi + L \frac{d\phi}{dT}, \quad (30)$$

where L is the latent heat of melting for the SiGe alloy, which is estimated as $L = xL_{\text{Ge}} + (1 - x)L_{\text{Si}}$ using Vegard's law. By incorporating the thermocapillary-driven convection with a velocity field \mathbf{u} , and a heat source, the final form of the heat transport equation in Eq. (29) can be written as

$$\rho c_p \left[\frac{dT}{dt} + \mathbf{u} \cdot \nabla T \right] = \nabla \cdot k \nabla T + Q. \quad (31)$$

Here, the external heat source Q , due to the volumetric absorption of the Gaussian laser beam, is given by the Beer–Lambert law in terms of the absorption coefficient α and laser intensity I as

$$Q = \alpha I(X, Y, Z) = \alpha \frac{2(1-R)P_0}{\pi r_0^2} e^{-2\alpha(X(t)^2 + Y^2)/r_0^2} e^{\alpha z}, \quad (32)$$

where $R = 0.4$ is the reflection coefficient, P_0 is the optical power, r_0 is the beam radius, and coordinate $X(t) = vt$ is given in terms of the time t and constant scan speed v .

The shape and size of the liquid/solid interface, as the boundary of the laser-induced molten zone, is completely represented by the phase-field ϕ , of which evolution drives the phase segregation and non-dendritic solidification. In non-isothermal conditions, where the temperature field $T(\mathbf{r}, t)$, significantly changes within the SiGe epilayer, the thickness of the mushy solid/liquid interface has a position-dependent value, because it is determined by the local temperature gradient ∇T , and the temperature range (mushy zone) between the liquidus and solidus curves in the phase diagram at a particular Ge content. For example, the mushy interface has the smallest thickness at the bottom of the molten zone close to the SiGe/Si interface, where the highest temperature gradient occurs. Therefore, instead of solving the Allen–Cahn equation in Eq. (18), which depends on the unknown gradient term ϵ_ϕ and mobility parameter M_ϕ , we found the time evolution of the phase-field ϕ by postulating its explicit temperature dependence and incorporating it into the heat transport equation via the apparent heat capacity in Eq. (30). In laser processing of SiGe on silicon substrates, the thermal gradient at the solidifying edge of the interface is very high ($>2.2 \times 10^9 \text{ K m}^{-1}$), which suppresses constitutional undercooling in the experimental scan speed range, and thus results in non-dendritic solidification. Therefore, we assumed that the phase-field $\phi(T)$ is an explicit function of the temperature T , smoothly rising from $\phi = 0$ (solid) to $\phi = 1$ (liquid) between the solidus temperature T_S and liquidus temperature T_L , which were calculated for the initial Ge molar fraction of $x_0 = 0.5$. The temperature derivative of ϕ in Eq. (30) is defined by a unit-area parabolic function, which moderates the capture and release of the latent heat as

$$\frac{d\phi}{dT} = \begin{cases} 0, & T < T_S \text{ (Solid phase)} \\ \frac{3}{2\Delta T} \left(1 - \frac{(T - T_m)^2}{(\Delta T/2)^2} \right), & T_S < T < T_L \text{ (Mushy zone)} \\ 0, & T > T_L \text{ (Liquid phase)} \end{cases}, \quad (33)$$

where $T_m = (T_S + T_L)/2$ is the melting temperature of the alloy, and $\Delta T = (T_L - T_S)$ is the temperature range for the mushy zone. In this way, the coupled evolution of temperature and phase-field parameter was determined by solving the heat transport equation in COMSOL. This helped us to reduce the number of differential equations as well as to formulate the phase-field model with variables completely governed by the known thermophysical properties of the SiGe alloys and laser processing parameters.

Data availability

The datasets generated during the current study are available in the University of Southampton Institutional Research Repository at <https://doi.org/10.5258/SOTON/D1701>.

Received: 13 October 2020; Accepted: 17 May 2021;

Published online: 11 June 2021

References

- Alferov, Z. I. Nobel Lecture: the double heterostructure concept and its applications in physics, electronics, and technology. *Rev. Mod. Phys.* **73**, 767–782 (2001).
- Paul, D. J. Si/SiGe heterostructures: from material and physics to devices and circuits. *Semicond. Sci. Technol.* **19**, R75–R108 (2004).
- Paul, D. J. The progress towards terahertz quantum cascade lasers on silicon substrates. *Laser Photonics Rev.* **4**, 610–632 (2010).
- Bhattacharya, P. K. & Dutta, N. K. Quantum well optical devices and materials. *Annu. Rev. Mater. Sci.* **23**, 79–123 (1993).
- Chaisakul, P. et al. Recent progress on Ge/SiGe quantum well optical modulators, detectors, and emitters for optical interconnects. *Photonics* **6**, 24 (2019).
- Tournié, E. & Trampert, A. MBE growth and interface formation of compound semiconductor heterostructures for optoelectronics. *Phys. Stat. Solidi* **244**, 2683–2696 (2007).
- Cai, Z., Liu, B., Zou, X. & Cheng, H.-M. Chemical vapor deposition growth and applications of two-dimensional materials and their heterostructures. *Chem. Rev.* **118**, 6091–6133 (2018).
- Isa, F. et al. Highly mismatched, dislocation-free SiGe/Si heterostructures. *Adv. Mater.* **28**, 884–888 (2016).
- Li, H., Wang, X., Zhu, X., Duan, X. & Pan, A. Composition modulation in one-dimensional and two-dimensional chalcogenide semiconductor nanostructures. *Chem. Soc. Rev.* **47**, 7504–7521 (2018).
- Zhang, Z. et al. Robust epitaxial growth of two-dimensional heterostructures, multiheterostructures, and superlattices. *Science* **357**, 788–792 (2017).
- Wu, Y., Fan, R. & Yang, P. Block-by-block growth of single-crystalline Si/SiGe superlattice nanowires. *Nano Lett.* **2**, 83–86 (2002).
- Fang, X. et al. Heterostructures and superlattices in one-dimensional nanoscale semiconductors. *J. Mater. Chem.* **19**, 5683–5689 (2009).
- Chueh, Y.-L. et al. Nanoscale structural engineering via phase segregation: Au-Ge system. *Nano Lett.* **10**, 393–397 (2010).
- Susarla, S. et al. Thermally induced 2D alloy-heterostructure transformation in quaternary alloys. *Adv. Mater.* **30**, 1804218 (2018).
- Wu, M. et al. Detecting lateral composition modulation in dilute Ga(As,Bi) epilayers. *Nanotechnology* **26**, 425701 (2015).
- Conti, M. Interface dynamics, instabilities, and solute bands in rapid directional solidification. *Phys. Rev. E* **58**, 2071–2078 (1998).
- Shiraki, Y. & Sakai, A. Fabrication technology of SiGe hetero-structures and their properties. *Surf. Sci. Rep.* **59**, 153–207 (2005).
- Olesinski, R. W. & Abbaschian, G. J. The Ge-Si (germanium-silicon) system. *Bull. Alloy Phase Diagr.* **5**, 180–183 (1984).
- Kurz, W. in *Fundamentals of Solidification* (ed. Fisher, D. J.) Ch. 3 (Trans Tech Publications, 1992).
- Miller, W., Abrosimov, N., Rasin, I. & Borissova, D. Cellular growth of Ge_{1-x}Si_x single crystals. *J. Cryst. Growth* **310**, 1405–1409 (2008).
- Gotoh, R. et al. Formation mechanism of cellular structures during unidirectional growth of binary semiconductor Si-rich SiGe materials. *Appl. Phys. Lett.* **100**, 021903 (2012).
- Mokhtari, M. et al. Instability of crystal/melt interface in Si-rich SiGe. *J. Appl. Phys.* **124**, 085104 (2018).
- Weizman, M., Nickel, N. H., Sieber, I. & Yan, B. Successive segregation in laser-crystallized poly-SiGe thin films. *J. Non-Cryst. Solids* **352**, 1259–1262 (2006).
- Kitahara, K., Hirose, K., Suzuki, J., Kondo, K. & Hara, A. Growth of quasi-single-crystal silicon-germanium thin films on glass substrates by continuous wave laser lateral crystallization. *Jpn J. Appl. Phys.* **50**, 115501 (2011).
- Gaiduk, P. I. & Prakopyeu, S. L. in *Subsecond Annealing of Advanced Materials* (eds. Skorupa, W. & Schmidt, H.) Ch. 5 (Springer, 2014).
- Ong, C. Y. et al. Laser annealing induced high Ge concentration epitaxial SiGe layer in Si_{1-x}Ge_x virtual substrate. *Appl. Phys. Lett.* **93**, 041112 (2008).
- Dagault, L. et al. Impact of UV nanosecond laser annealing on composition and strain of undoped Si_{0.8}Ge_{0.2} epitaxial layers. *ECS J. Solid State Sci. Technol.* **8**, P202–P208 (2019).
- Aktas, O. et al. Laser-driven phase segregation and tailoring of compositionally graded microstructures in Si–Ge nanoscale thin films. *ACS Appl. Mater. Interfaces* **12**, 9457–9467 (2020).
- Tiller, W. A., Jackson, K. A., Rutter, J. W. & Chalmers, B. The redistribution of solute atoms during the solidification of metals. *Acta Metall.* **1**, 428–437 (1953).
- Coucheron, D. A. et al. Laser recrystallization and inscription of compositional microstructures in crystalline SiGe-core fibres. *Nat. Commun.* **7**, 13265 (2016).
- Chen, L.-Q. Phase field models for microstructure evolution. *Annu. Rev. Mater. Res.* **32**, 113–140 (2002).
- Warren, J. A. & Boettinger, W. J. Prediction of dendritic growth and microsegregation patterns in a binary alloy using the phase-field method. *Acta Metall. Mater.* **43**, 689–703 (1995).
- Moelans, N., Blanpain, B. & Wollants, P. An introduction to phase-field modeling of microstructure evolution. *Comput. Coupling Phase Diagr. Thermochem.* **32**, 268–294 (2008).
- Lin, H. K., Chen, H. Y. & Lan, C. W. Adaptive phase field modeling of morphological instability and facet formation during directional solidification of SiGe alloys. *J. Cryst. Growth* **385**, 44–48 (2014).
- Lockwood, D. J. et al. Si/SiGe heterointerfaces in one-, two-, and three-dimensional nanostructures: their impact on SiGe light emission. *Front. Mater.* **3**, 12 (2016).
- Ballabio, A. et al. Ge/SiGe parabolic quantum wells. *J. Phys. D* **52**, 415105 (2019).
- Yamamoto, Y. et al. Ge/SiGe multiple quantum well fabrication by reduced-pressure chemical vapor deposition. *Jpn J. Appl. Phys.* **59**, SGK10 (2020).

38. Barrिताult, P. et al. Mlines characterization of the refractive index profile of SiGe gradient waveguides at 2.15 μm . *Opt. Express* **21**, 11506–11515 (2013).
39. Rho, H., Jackson, H. E. & Weiss, B. L. Mapping of local stress distributions in SiGe/Si optical channel waveguide. *J. Appl. Phys.* **90**, 276–282 (2001).
40. Brun, M. et al. Low loss SiGe graded index waveguides for mid-IR applications. *Opt. Express* **22**, 508–518 (2014).
41. Ramirez, J. M. et al. Graded SiGe waveguides with broadband low-loss propagation in the mid infrared. *Opt. Express* **26**, 870–877 (2018).
42. Wang, X. et al. Nanosecond laser writing of straight and curved waveguides in silicon with shaped beams. *J. Laser Appl.* **32**, 022002 (2020).
43. Martinez-Jimenez, G. et al. Photonic micro-structures produced by selective etching of laser-crystallized amorphous silicon. *Opt. Mater. Express* **9**, 2573–2581 (2019).
44. Liu, Q. et al. On-chip Bragg grating waveguides and Fabry-Perot resonators for long-wave infrared operation up to 8.4 μm . *Opt. Express* **26**, 34366–34372 (2018).
45. Ams, M., Dekker, P., Gross, S. & Withford, M. J. Fabricating waveguide Bragg gratings (WBGs) in bulk materials using ultrashort laser pulses. *Nanophotonics* **6**, 743–763 (2017).
46. Scappucci, G. et al. The germanium quantum information route. *Nat. Rev. Mater.* <https://doi.org/10.1038/s41578-020-00262-z> (2020).
47. Igo, J., Gabel, M., Yu, Z.-G., Yang, L. & Gu, Y. Photodefined in-plane heterostructures in two-dimensional In_2Se_3 nanolayers for ultrathin photodiodes. *ACS Appl. Nano Mater.* **2**, 6774–6782 (2019).
48. Bi, Z. & Sekerka, R. F. Phase-field model of solidification of a binary alloy. *Phys. A* **261**, 95–106 (1998).
49. Boettinger, W. J., Warren, J. A., Beckermann, C. & Karma, A. Phase-field simulations of solidification. *Annu. Rev. Mater. Res.* **32**, 163–194 (2002).
50. De Oliveira, M. J. Binary mixtures in *Equilibrium Thermodynamics* (eds. Rhodes, W. T., Stanley, H. E. & Needs, R.) Ch. 10 (Springer, 2013).
51. Chan, C. L., Mazumder, J. & Chen, M. M. Effect of surface tension gradient driven convection in a laser melt pool: three-dimensional perturbation model. *J. Appl. Phys.* **64**, 6166–6174 (1988).
52. Zhang, Q. Z. et al. Numerical investigation on selective emitter formation by laser doping for phosphorous-doped silicon solar cells. *J. Laser Appl.* **29**, 022003 (2017).
53. Ricci, E. et al. Surface tension and density of Si-Ge melts. *J. Chem. Phys.* **140**, 214704 (2014).
54. Penrose, O. & Fife, P. C. Thermodynamically consistent models of phase-field type for the kinetics of phase transitions. *Phys. D* **43**, 44–62 (1990).
55. Steinbach, I. Phase-field models in materials science. *Model. Simul. Mater. Sci. Eng.* **17**, 073001 (2009).

Acknowledgements

The authors acknowledge the use of the IRIDIS-5 High-Performance Computing Facility at the University of Southampton, and support of the Engineering and Physical Sciences

Research Council (EPSRC) (EP/P000940/1 and EP/N013247/1) for the completion of this work.

Author contributions

O.A. and A.C.P. conceived the research. O.A. conducted the simulations and theoretical calculations. Y.Y. and M.K. prepared the epitaxially grown SiGe/Si samples and conducted STEM/EDX analysis. O.A. performed the laser processing of the SiGe samples, their imaging by optical microscopy, and optical coupling experiments for the laser-written graded-index waveguides. O.A. and A.C.P. interpreted the results and wrote the manuscript. All authors contributed to the discussion and review.

Competing interests

The authors declare no competing interests.

Additional information

Supplementary information The online version contains supplementary material available at <https://doi.org/10.1038/s42005-021-00632-1>.

Correspondence and requests for materials should be addressed to O.A. or A.C.P.

Peer review information Communications Physics thanks the anonymous reviewers for their contribution to the peer review of this work. Peer reviewer reports are available.

Reprints and permission information is available at <http://www.nature.com/reprints>

Publisher's note Springer Nature remains neutral with regard to jurisdictional claims in published maps and institutional affiliations.



Open Access This article is licensed under a Creative Commons Attribution 4.0 International License, which permits use, sharing, adaptation, distribution and reproduction in any medium or format, as long as you give appropriate credit to the original author(s) and the source, provide a link to the Creative Commons license, and indicate if changes were made. The images or other third party material in this article are included in the article's Creative Commons license, unless indicated otherwise in a credit line to the material. If material is not included in the article's Creative Commons license and your intended use is not permitted by statutory regulation or exceeds the permitted use, you will need to obtain permission directly from the copyright holder. To view a copy of this license, visit <http://creativecommons.org/licenses/by/4.0/>.

© The Author(s) 2021